Progress In Electromagnetics Research C, Vol. 90, 209–224, 2019

Virtual Synchronous Motor Dynamic Power Decoupling Strategy

Xintian Liu, Yucai Li*, Yao He, Xinxin Zheng, and Guojian Zeng

Abstract—Due to the existence of power coupling the virtual synchronous motor (VSG) will lead to overshoot fluctuations in the power adjustment process, thus affecting the control performance. Compared to the traditional direct current control inverter based on coordinate transformation, VSG model is more complex and difficult to achieve decoupling. This paper presents a dynamic power decoupling method by studying the coupling relationship between active power and reactive power of VSG. Firstly, the inverter grid-connected model is established, and the power expression is analyzed when the inverter output impedance is negligible. Then the virtual active power and reactive power expressions are obtained through coordinate transformation. Several key state equations and virtual states of the VSG are obtained. The power expression performs small signal perturbation to obtain the dynamic model of the VSG. From this, the dynamic model of the VSG can be analyzed to obtain the coupling relationship between the dynamic powers, and the series power compensation is used to decouple the dynamic power coupling. Finally, the correctness of the theoretical analysis and the effectiveness of the decoupling method are verified by simulation and experiments.

1. INTRODUCTION

Nowadays, energy crisis and environmental problems are becoming more and more serious. Distributed generation technology is an effective means to solve this problem [1]. In traditional power systems, power grid connection is realized by synchronous machines [2]. With more and more distributed energy integrated into the power grid [3], the structure of a traditional power system is affected so that the distributed energy needs to achieve power regulation [4], and the concept of virtual synchronous generator (VSG) is proposed [5]. VSG fully simulates the characteristics of synchronous motors and is expected to be an effective way to solve the security problems caused by large amounts of distributed energy interconnection. Since its concept was put forward, it has attracted much attention [6–11].

The research on VSG is mainly focused on the improvement of inverter control performance. Reference [9] points out that the phase-locked loop can be omitted in the control system because of the synchronization characteristics of virtual synchronous motor, so that the whole control system structure is simplified, and the system performance is greatly improved. Reference [10] shows that active and reactive loops are approximately decoupled after small signal modeling, so the parameters of active and reactive loops can be designed separately, which greatly simplifies the parameter design. Reference [11] proposes a method of adding damping correction loop in VSG algorithm, which adds a parameter to the damping coefficient. By adjusting this parameter, the response speed of power regulation can be improved.

However, these methods do not consider the coupling between active power and reactive power. In [9], the coupling between active and reactive powers is not considered, resulting in coupling power fluctuation and steady-state error in power regulation. The parameter design method is proposed in [10] when the inductance is much larger than the resistance, i.e., $X \gg R$. The authors analyze that the

Received 25 October 2018, Accepted 26 December 2018, Scheduled 5 March 2019
* Corresponding author: Yucai Li (yucai.li2016@foxmail.com).
The authors are with the Hefei University of Technology, Hefei, China.

active power and reactive power are approximately decoupled when the inductance is much larger than the resistance $X \gg R$, but the power is not completely decoupled at this time. The authors only make an approximate analysis, so the power coupling is still dynamic. State characteristics are influential. The optimization method of virtual synchronous motor control proposed in [11] is also based on the condition that the inductance is much larger than the resistance $X \gg R$. It is pointed out that the coupling effect of power regulation after adding damping correction loop is weakened properly, but the reasons are not analyzed in depth.

Aiming at the decoupling problem, most of the current-controlled inverters based on coordinate transformation are studied. Reference [12] aims at the coupling between the dq axes of LCL filter grid-connected inverters. The components of other axes information are injected into each axis controller, and the components injected are equal to the coupling magnitude produced by the controlled object, but the direction is reversed, so that decoupling can be realized. Reference [13] also studies the dynamic coupling between the dq axes of the LCL grid-connected inverter. Three-loop feedback compensation method is used to effectively suppress the coupling overshoot in the process of dynamic power regulation. However, for VSG, its model is so complex that the decoupling is difficult to achieve. At present, most of the decoupling research on VSG is static coupling [14–16]. There are few studies on dynamic coupling. Reference [17] analyzes the dynamic coupling between active power P and reactive power Q according to the instantaneous power theory. However, due to the complexity of the model used, the coupling relationship is also complicated, and the main reason of affecting the dynamic coupling is not pointed out, so this model is not suitable for decoupling research.

In view of the above problems, the VSG dynamic coupling model established in this paper has a clear structure, which can effectively solve the problem that the VSG coupling model is complex and difficult to analyze the coupling causes, and has the advantage of easy decoupling.

Firstly, the basic principle of VSG is analyzed, and then the static coupling relationship between active power and reactive power of virtual synchronous motor is analyzed according to the circuit theory. The expression of virtual active power and reactive power is obtained by coordinate transformation. On this basis, the dynamic coupling of the system is modeled and analyzed by small signal analysis method, and the decoupling in the dynamic regulation process is realized by series compensation method. Finally, the theoretical analysis is verified by simulation and experiment.

2. COUPLING CHARACTERISTICS OF VSG

2.1. VSG Power Loop and Its Control Strategy

VSG DC-side voltage V_{in} is defined. Inverters are converted into three-phase alternating current by a three-phase bridge arm and an LC filter. u_{abc} and i_{abc} are output voltage and current of inverter. The output active power P and reactive power Q of the inverter can be calculated by the instantaneous power theory [18] after the transformation of u_{abc} and i_{abc} by Park. The expression is

$$\begin{cases} P = \dfrac{3}{2}(u_d i_d + u_q i_q) \\ Q = \dfrac{3}{2}(u_q i_d - u_d i_q) \end{cases} \tag{1}$$

In the formula, u_d and u_q are the active and reactive components of u_{abc} in a dq coordinate system after Park transformation. i_d and i_q are the active and reactive components of i_{abc}. The whole control system consists of inner loop and outer loop. The outer loop is VSG algorithm as shown in Figure 1 [5]. The inner loop is PR controller.

VSG algorithm mainly includes active power control loop and reactive power control loop. Active power loop mainly realizes active-frequency control, simulates the rotor motion equation of synchronous motor, realizes primary frequency modulation and inertia regulation, while reactive power-voltage control loop mainly simulates the excitation equation of the synchronous motor and realizes the primary voltage regulation characteristic of the synchronous motor. According to Figure 1, the main equations of VSG can be obtained as shown below

$$J\frac{d\omega}{dt} = T_{set} - T - D_p(\omega - \omega_n) \tag{2}$$

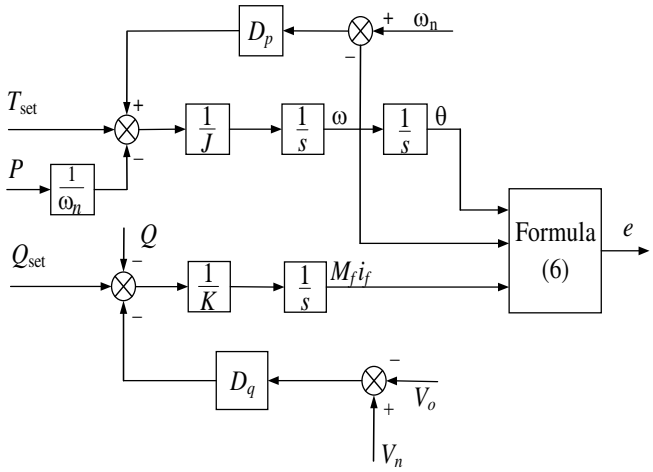

Figure 1. VSG algorithm.

$$\theta = \int \omega dt \tag{3}$$

$$T = \frac{P}{\omega_n} \tag{4}$$

$$K\frac{dM_f i_f}{dt} = Q_{set} - Q + D_q(V_n - V_o) \tag{5}$$

In the formula, J is the moment of inertia, D_p the damping coefficient, ω_n the mesh side synchronous angular velocity, ω the reference angular velocity, T_{set} the mechanical torque, T the electromagnetic torque, K the integral coefficient, Q_{set} the set value of reactive power, Q the output reactive power of inverter, D_q the droop coefficient of reactive loop, V_n the rated voltage amplitude, and V_o the output voltage amplitude of inverter.

According to the active power loop, the phase angle θ and angular velocity ω can be calculated, and the voltage information $M_f i_f$ can be calculated by the reactive power loop. The electromotive force reference value e transmitted to the inner loop of the VSG loop can be calculated as shown in Equation (6).

$$\begin{cases} e_a = M_f i_f \omega \sin\theta \\ e_b = M_f i_f \omega \sin\left(\theta - \dfrac{2\pi}{3}\right) \\ e_c = M_f i_f \omega \sin\left(\theta - \dfrac{4\pi}{3}\right) \end{cases} \tag{6}$$

In order to improve the tracking accuracy [19], the inner loop adopts the PR controller, and the filtered inductor current signal is used as the control amount. According to the LC filter circuit structure, the following formula can be obtained.

$$e - u_o = L\frac{di}{dt} + iR \tag{7}$$

where e is the inverter terminal voltage, u_o the inverter output voltage, L the filter inductor, R the parasitic resistance, and i the inductor current. Calculate the reference value i of the inductor current i_l according to Equation (7), and then obtain the error signal by collecting the inductor current in the circuit. The error signal is sent to the inner loop PR controller, and the PR controller can perform no-difference control on the AC signal.

$$G_{PR}(s) = K_P + \frac{2K_r s}{s^2 + \omega_o^2} \tag{8}$$

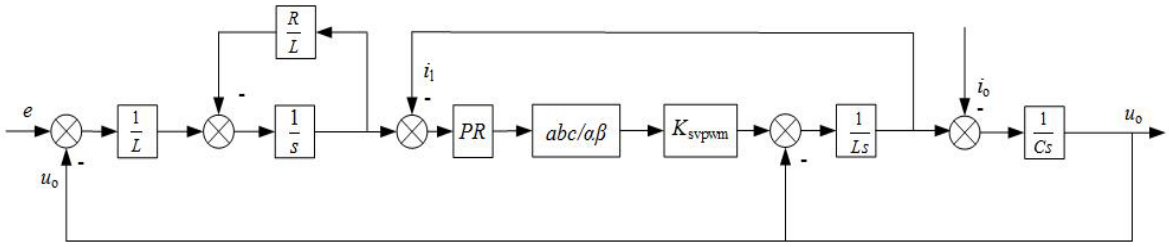

Figure 2. The struct graphic of whole system.

where K_p is the proportional coefficient, K_r the resonance coefficient, and ω_0 the resonant frequency. The error signal is passed through the PR controller to obtain the SVPWM signal for driving the IGBT, and the whole control system structure is shown in Figure 2.

2.2. Coupling Analysis

In order to analyze the dynamic coupling characteristics of the VSG, the first step must be to obtain a dynamic coupling model of the VSG.

Figure 3 shows the power flow graph of the inverter grid-connected circuit considering the inverter output impedance and grid-connected line impedance. In Figure 3, Z_o is the inverter system output impedance, Z the grid-connected line impedance, E the inverter output voltage, and its phase angle is δ. U is the grid side voltage, and its phase angle is 0.

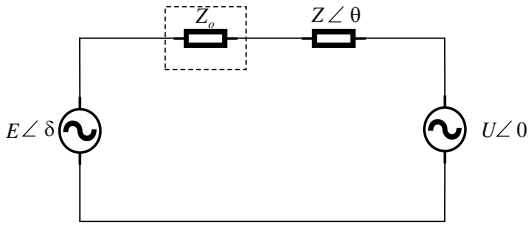

Figure 3. The graphic of power flow.

According to the structure diagram shown in Figure 2, the expression of Z_o can be obtained. Let the transfer function of K_{SVPWM} in Figure 2 be $G_{SVPWM}(s)$, and the gain expression can be expressed by the following formula [20].

$$G_{SVPWM}(s) = \frac{(1.5T_s)^2 s^2 - 6(1.5T_s)s + 12}{(1.5T_s)^2 s^2 + 6(1.5T_s)s + 12} \tag{9}$$

where T_s is the switching period of SVPWM, so Z_o can be obtained from the Mason gain formula.

$$Z_o = \frac{u_o}{i_o} = \frac{-(Ls+R)Ls}{(LCs^2+1)(Ls+R) + G_{PR}(s)G_{SVPWM}(s)(LCs^2+CRs+1)} \tag{10}$$

According to the relevant parameters of Table 1, the Bode diagram of Z_o can be obtained as shown in Figure 4. It can be seen from Figure 4 that the amplitude of the system impedance is very small at the power frequency of 50 Hz, so when calculating the impedance of the grid connection line can ignore the output impedance of the system. At this time, the impedance of the grid in the power flow diagram shown in Figure 3 is only Z, and there are $Z\angle\theta = R + jX$, where R and X are the grid-connected line resistance and inductive reactance, so the power injected into the grid can be expressed below.

$$\begin{cases} P = \dfrac{E}{R^2+X^2}[R(E - U\cos\delta) + XU\sin\delta] \\ Q = \dfrac{E}{R^2+X^2}[-RU\sin\delta + X(E - U\cos\delta)] \end{cases} \tag{11}$$

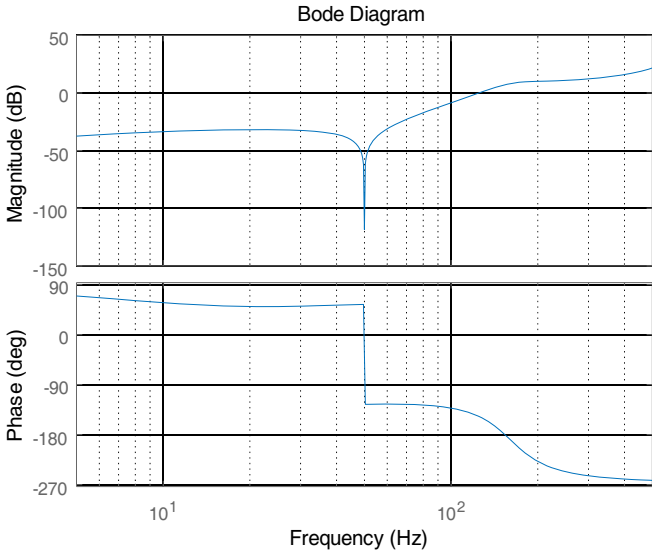

Figure 4. The bode graphic of system impedance.

Table 1. Three-phase VSG parameters.

Parameter	value
Input voltage U_{in}/V	700
Grid voltage U_g/V	220
Output power P_o/kW	10
Power frequency f/Hz	50
P-F droop coefficient D_p	8
Damping coefficient J	0.001
Reactive loop coefficient K	10000
Resonance coefficient K_r	300
Filter Inductor L_1/mH	1.285
Parasitic resistance R_1/Ω	0.3
Filter capacitor C/uF	50
Grid-connected inductor L_2/mH	1.285
Grid-connected resistor R/Ω	0.3
Q-U drooping coefficient D_q	321
Proportion factor K_p	0.5
Steady state power angle δ_n	0.005

If the small signal is directly made at this time, the obtained dynamic coupling model will be too complicated, which makes decoupling difficult to implement. Therefore, the coordinate transformation can be done first to obtain the virtual work expression, and the transformation method is as follows [21]

$$\begin{cases} P' = P\sin\theta - Q\cos\theta \\ Q' = P\cos\theta + Q\sin\theta \end{cases} \tag{12}$$

where θ is the impedance angle of the grid-connected line, and $\cos\theta = R/Z$, $\sin\theta = X/Z$ [22].

Equation (13) can be obtained by Equations (11) and (12)

$$\begin{cases} P' = \dfrac{EU\sin\delta}{Z} \\ Q' = \dfrac{E(E - U\cos\delta)}{Z} \end{cases} \tag{13}$$

In the formula, δ is the power transmission angle of the grid connection, which can be obtained by the following formula

$$\delta = \int \omega - \omega_g dt \tag{14}$$

In the formula, ω is the inverter output voltage angular frequency, and ω_g is the grid side voltage angular frequency.

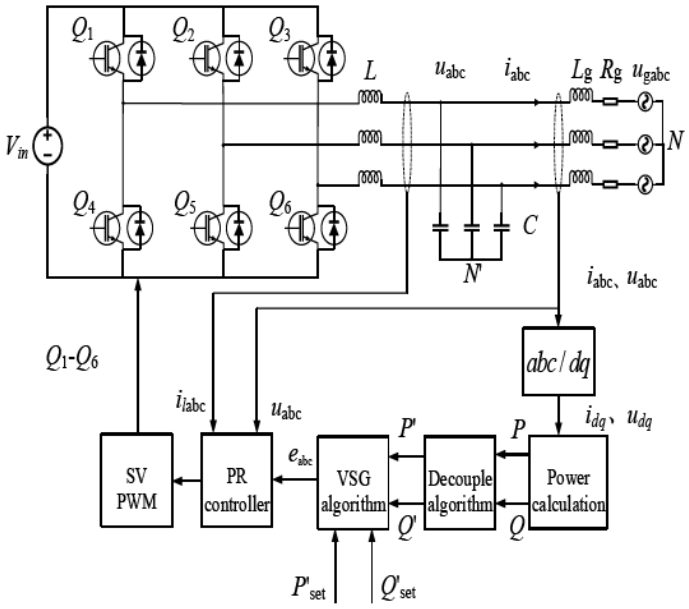

Figure 5. The main circuit graphic with virtual power.

Figure 5 shows the structure of the main circuit after the coordinate transformation is added. At this time, the power fed back to the VSG algorithm is the virtual active and reactive powers, so the power values in Equations (2) and (5) also become virtual power, as follows

$$J\frac{d\omega}{dt} = \frac{P'_{set}}{\omega} - \frac{P'}{\omega} - D_p(\omega - \omega_n) \tag{15}$$

$$K\frac{dM_f i_f}{dt} = Q'_{set} - Q' + D_q(V_n - V_o) \tag{16}$$

At this point, the small-signal analysis can be used to obtain the dynamic coupling model of the system. Perform small signal disturbances on the variables E, δ, P', Q', P'_{set}, Q'_{set}, ω, $M_f i_f$ in Equations (6), (13)–(16), then eliminate the DC amount on both sides of the equation, ignore the disturbance amount of more than two times [23], and consider the approximate relationship $\cos\hat{\delta} \approx 1$, $\sin\hat{\delta} \approx \hat{\delta}$ to obtain the following equation, where δ_n is the power angle at steady state.

$$\frac{\hat{P}'_{set}}{\omega_n} - D_p\hat{\omega} - \frac{\hat{P}'}{\omega_n} = J\frac{d\hat{\omega}}{dt} \tag{17}$$

$$\hat{Q}'_{set} - D_q\hat{E} - \hat{Q}' = K\frac{d\hat{M_f i_f}}{dt} \tag{18}$$

$$\hat{\delta} = \int \hat{\omega} dt \tag{19}$$

$$\hat{E} \approx \omega_n \hat{M_f} i_f + \hat{\omega_n} \tag{20}$$

$$\hat{P'} = \frac{3UE}{Z} \cos\delta_n \hat{\delta} + \frac{3U}{Z} \sin\delta_n \hat{E} \tag{21}$$

$$\hat{Q'} = \frac{3(2E - U\cos\delta_n)}{Z} \hat{E} + \frac{3EU}{Z} \sin\delta_n \hat{\delta} \tag{22}$$

The Laplace transform of Equations (17)–(19) yields the following equation

$$\frac{\hat{P'}_{set}}{\omega_n} - \frac{\hat{P'}}{\omega_n} = (Js + D_p)\hat{\omega} \tag{23}$$

$$\hat{Q'}_{set} - \hat{Q'} = (Ks + D_q)\hat{M_f} i_f \tag{24}$$

$$\hat{\delta} = \frac{1}{s}\hat{\omega} \tag{25}$$

According to Eqs. (20)–(25), the dynamic coupling model structure diagram can be obtained as shown in Figure 6. The coupling relationship between the active power loop and reactive power loop can be seen, and the coupling amount is related to the voltage amplitude E, steady state power angle δ_n, and grid-connected impedance Z.

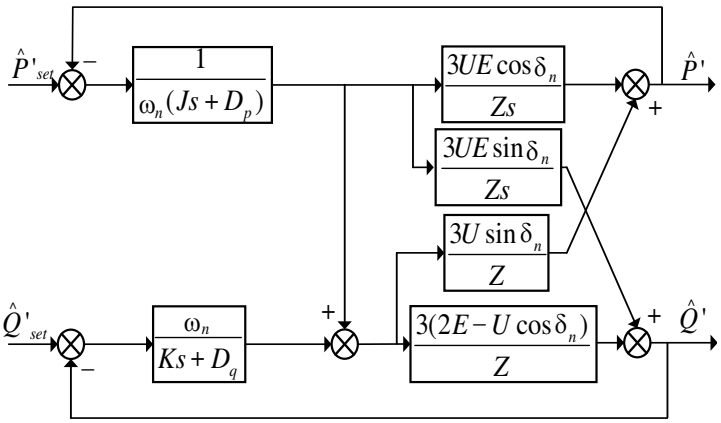

Figure 6. The dynamical coupling model.

3. DECOUPLING STRATEGY

For the coupling structure diagram shown in Figure 6, series compensation can be introduced to decouple the dynamic coupling.

The system shown in Figure 7 is a system with a simplified structure of the dynamic coupling model of Figure 6 and introduced into the series compensation system. The system is a two-input and two-output system. If the closed loop of the system can be decoupled, the open-loop transfer function is a diagonal array [24], i.e., the output of the input $X_1(s)$ to $Y_2(s)$ in the dotted line frame is 0, and the output of the input $X_2(s)$ to $Y_1(s)$ is also 0. From the figure, it can be concluded that the input $X_1(s)$ to $Y_2(s)$ output is zero and needs to meet the following formula.

$$G_{c21}(s)G_2(s) + G_{21}(s) + G_2(s) = 0 \tag{26}$$

Can be solved

$$G_{c21}(s) = -[G_{21}(s) + G_2(s)]/G_2(s) \tag{27}$$

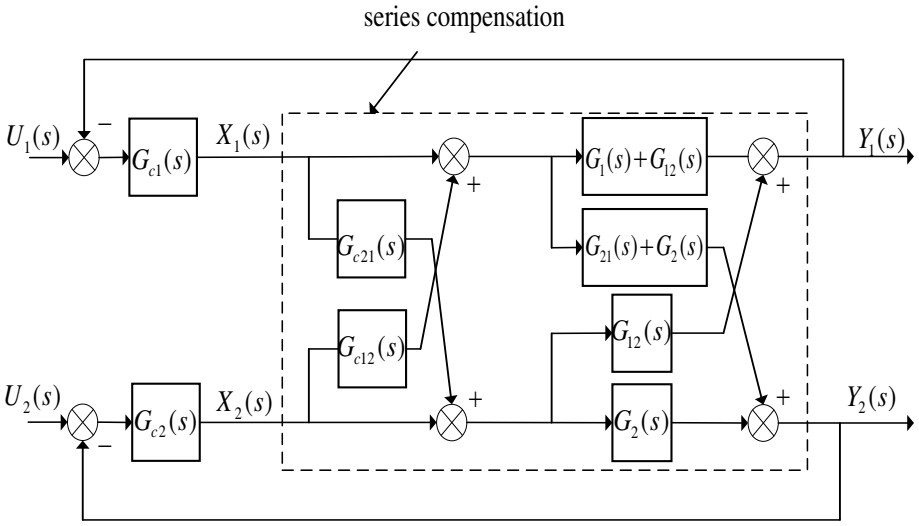

Figure 7. The struct graphic with series compensation.

For the same reason, the output of input $X_2(s)$ to $Y_1(s)$ is zero, and the following formula needs to be satisfied.

$$G_{c12}(s)[G_1(s) + G_{12}(s)] + G_{12}(s) = 0 \tag{28}$$

Equation (29) can be derived from Equation (28).

$$G_{c12}(s) = -G_{12}(s)/[G_1(s) + G_{12}(s)] \tag{29}$$

Therefore, the structure diagram shown in Figure 6 can be solved according to series compensation.

$$G_{c21}(s) = -\frac{3UE\sin\delta_n}{Zs}\frac{Z}{3(2E - U\cos\delta_n)} - 1 \tag{30}$$

VSG generally has $E \approx U$ in power regulation, so Equation (30) can be simplified to

$$G_{c21}(s) \approx -\frac{E\sin\delta_n}{s(2 - \cos\delta_n)} - 1 \tag{31}$$

where E is the maximum value of the inverter output voltage of 311 V, and δ_n is the power angle at steady state, which can be obtained by integrating the difference between the inverter output voltage angular frequency and the grid voltage angular frequency.

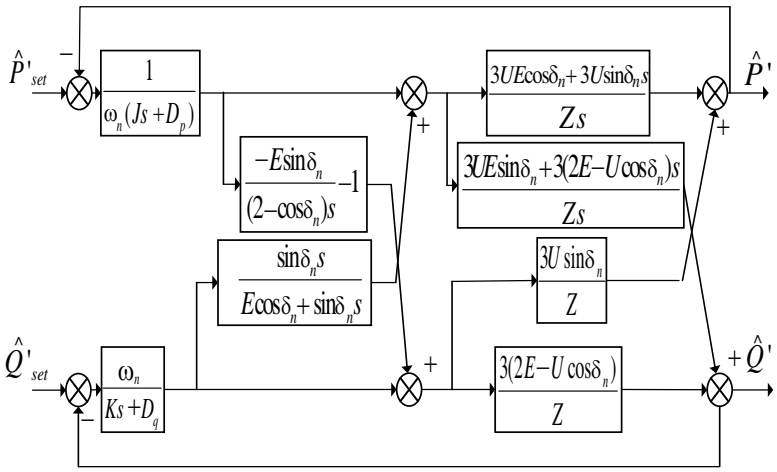

Figure 8. The dynamical model with series compensation added.

Equation (32) can be derived for the same reason

$$G_{c12}(s) = -\frac{3U\sin\delta_n}{Z}\frac{Zs}{3UE\cos\delta_n + 3U\sin\delta_n s} \tag{32}$$

From $U \approx E$, Equation (32) can be simplified to

$$G_{c12}(s) \approx -\frac{\sin\delta_n s}{E\cos\delta_n + s\cos\delta_n} \tag{33}$$

Equations (31) and (33) are the compensation amounts of the dynamic decoupling described in this paper. Figure 8 shows the system structure diagram after adding the series compensation to the VSG dynamic model.

4. SYSTEM STABILITY ANALYSIS

4.1. Active Loop Stability

The small-signal model shown in Figure 6 can be viewed as a two-input two-output system. When analyzing the performance of the active loop, the reactive power signal can be regarded as a disturbance signal and set to zero [25], so the small-signal model shown in Figure 6 can be simplified to Figure 9. According to Figure 9, the active power closed-loop transfer function can be obtained.

$$G(s)_{rpl} = \frac{a_1 s^2 + b_1 s + c_1}{d_1 s^3 + e_1 s^2 + f_1 s + g_1} \tag{34}$$

Among them

$$\begin{cases} a_1 = 3UZK\sin\delta_n \\ b_1 = 3UD_qZ\sin\delta_n + 3UEZK\cos\delta_n + 9U\omega_n(2E - U\cos\delta_n)\sin\delta_n \\ c_1 = 3UE\cos\delta_n ZD_q + 9UE\cos\delta_n\omega_n(2E - U\cos\delta_n) - 9U^2E\sin^2\delta_n\omega_n \\ d_1 = Z^2K\omega_nJ \\ e_1 = Z^2K\omega_nD_p + \omega_nJZ^2D_q + 3(2E - U\cos\delta_n)\omega_n^2JZ + 3U\sin\delta_nZK \\ f_1 = \omega_nD_pZ^2D_q + 3Z\omega_n^2D_p(2E - U\cos\delta_n) + 3U\sin\delta_nD_qZ \\ \quad\quad +3UEZK\cos\delta_n + 9U\sin\delta_n\omega_n(2E - U\cos\delta_n) \\ g_1 = 3UE\cos\delta_n ZD_q + 9UE\cos\delta_n\omega_n(2E - U\cos\delta_n) - 9U^2E\sin^2\delta_n\omega_n \end{cases} \tag{35}$$

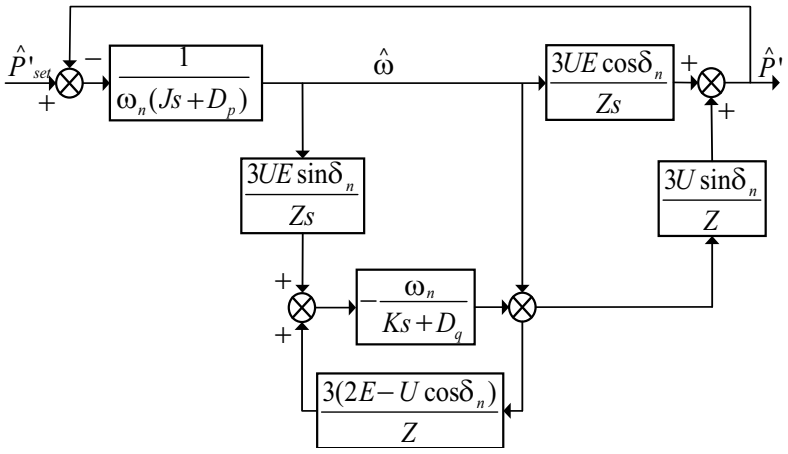

Figure 9. The simplified schematic of active power loop.

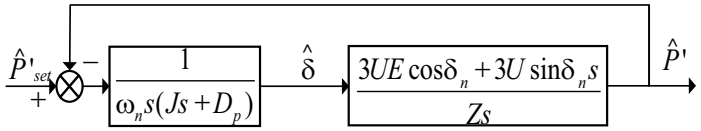

Figure 10. The schematic of decoupling active power loop.

When the series compensation decoupling is added, the active power loop graph can be obtained as shown in Figure 10, and the closed loop transfer function of the active loop is

$$G(s)_{dapl} = \frac{3UE\cos\delta_n + 3U\sin\delta_n s}{Z\omega_n Js^2 + (\omega_n D_p Z + 3U\sin\delta_n)s + 3UE\cos\delta_n} \tag{36}$$

It can be found that the closed loop pole of the active loop at this time is

$$Z_{adpl} = \frac{-(\omega_n D_p Z + 3U\sin\delta_n) \pm \sqrt{(\omega_n D_p Z + 3U\sin\delta_n)^2 - 12Z\omega_n JUE\cos\delta_n}}{2Z\omega_n J} \tag{37}$$

$$4ac = 12Z\omega_n JUE\cos\delta_n \tag{38}$$

In formula (38), δ_n does not exceed 90 degrees [10] when it is connected to the grid, so that Equation (38) greater than zero is constant, i.e., the closed loop pole of the active loop after decoupling is always located in the left half axis after series compensation, and the active loop remains stable for any parameter changes.

The root trajectory changes when the impedance Z transform is not decoupled and decoupled are shown in Figures 11(a) and 11(b). As shown, the poles of the undecoupled state and decoupled state are distributed on the left side of the 0 axis, i.e., the stability of the active loop after series compensation does not change.

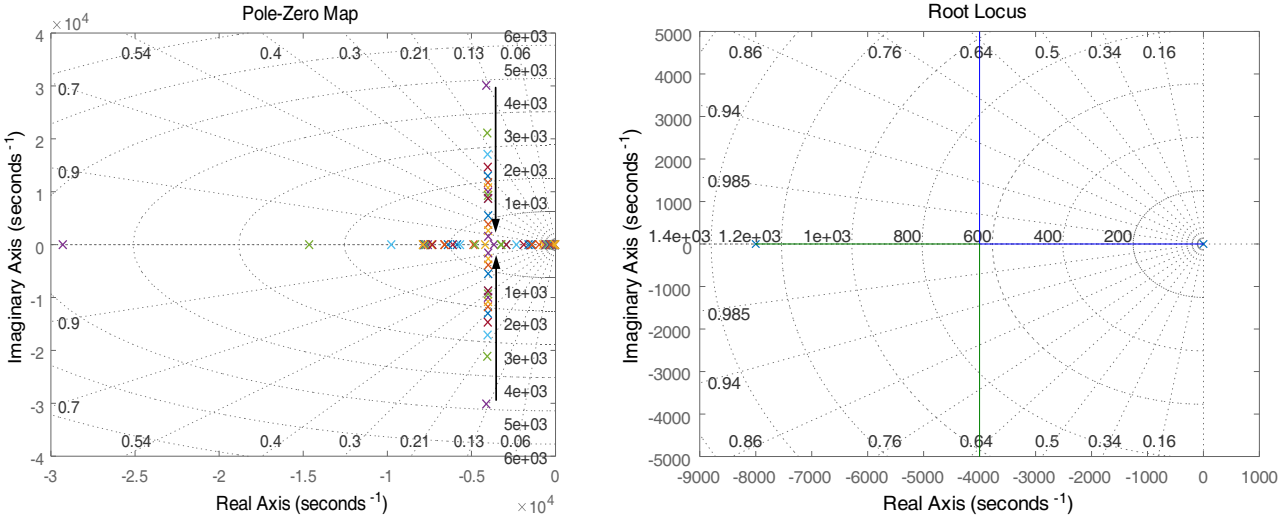

(a) (b)

Figure 11. Active power loop root locus. (a) The root locus in undecoupled mode with Z changed. (b) The root locus plot in decoupled mode with Z changed.

4.2. Reactive Loop Stability

Similarly, for the two-input and two-output system shown in Figure 6, when analyzing the reactive undecoupled loop, the active power reference can be regarded as a disturbance and set to zero. At this time, the reactive loop is simplified as shown in Figure 12.

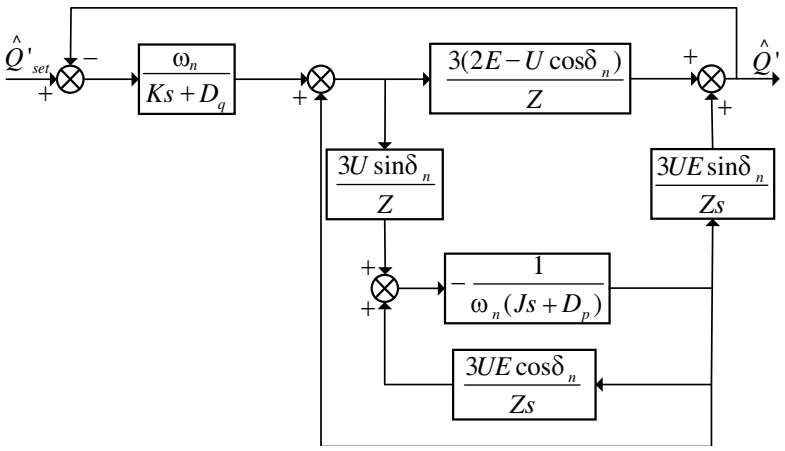

Figure 12. The simplified schematic of reactive power loop.

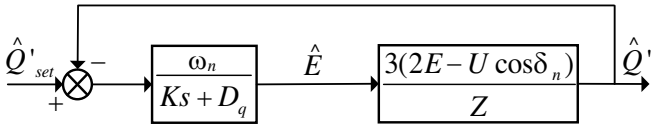

Figure 13. The schematic of decoupling reactive power loop.

According to Figure 12, the reactive power transfer function at this time can be obtained as

$$G(s)_{rpl} = \frac{a_2 s^2 + b_2 s + c_2}{d_2 s^3 + e_2 s^2 + f_2 s + g_2} \tag{39}$$

Among them

$$\begin{cases} a_2 = 3\omega_n^2 JZ(2E - U\cos\delta_n) \\ b_2 = 3\omega_n^2 D_p Z(2E - U\cos\delta_n) \\ c_2 = 9\omega_n UE\cos\delta_n(2E - U\cos\delta_n) - 9U^2 E\omega_n \sin^2\delta_n \\ d_2 = Z^2 K\omega_n J \\ e_2 = 3UZK\sin\delta_n + Z^2\omega_n JD_q + Z^2 K\omega_n D_p + 3\omega_n^2 JZ(2E - U\cos\delta_n) \\ f_2 = Z^2\omega_n D_p D_q + 3UEZK\cos\delta_n + 3U\sin\delta_n ZD_q + 3\omega_n^2 D_p Z(2E - U\cos\delta_n) \\ g_2 = 3UE\cos\delta_n ZD_q + 9\omega_n UE\cos\delta_n(2E - U\cos\delta_n) - 9U^2 E\omega_n \sin^2\delta_n \end{cases} \tag{40}$$

The reactive power loop after adding series compensation decoupling is shown in Figure 13. At this time, the closed loop transfer function of the reactive loop is

$$G(s)_{drpl} = \frac{3\omega_n(2E - U\cos\delta_n)}{KZs + D_q Z + 3\omega_n(2E - U\cos\delta_n)} \tag{41}$$

The closed loop pole of the reactive loop is

$$Z_{drpl} = -\frac{D_q Z + 3\omega_n(2E - U\cos\delta_n)}{KZ} \tag{42}$$

It can be seen from Equation (42) that the closed loop pole of the reactive loop at this time is always true for any parameter change pole less than 0, which means that the reactive loop is stable for any parameter change.

The root trajectory of the reactive power loop undecoupled state and the series compensation decoupling state with impedance Z changed are shown in Figures 14(a) and 14(b). The comparison graph shows that adding series compensation does not change the system stability. When there are

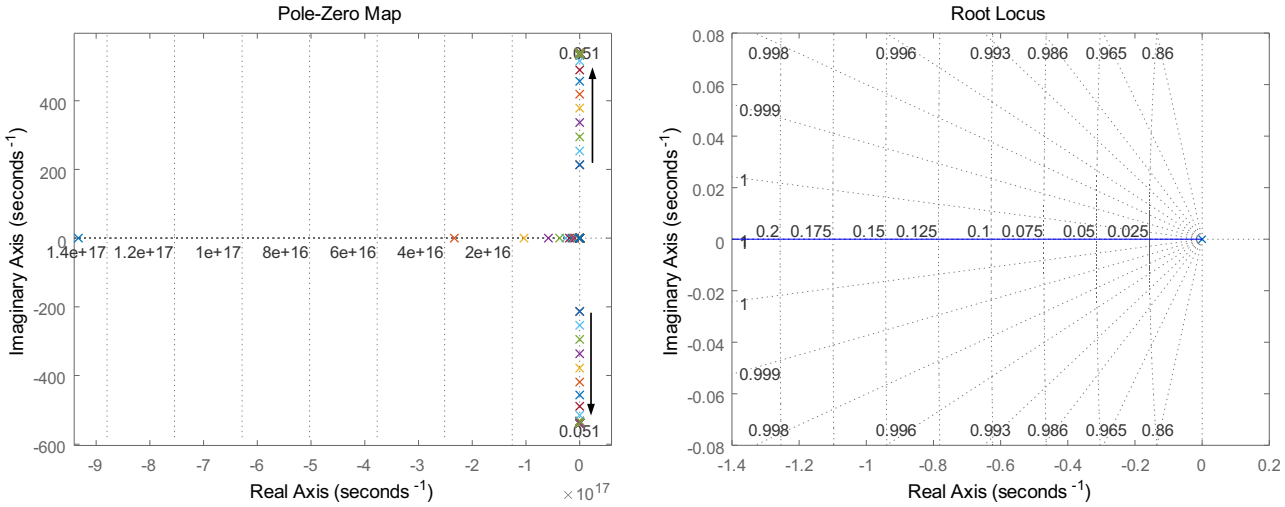

(a) (b)

Figure 14. Reactive power loop root locus. (a) The root locus plot in undecoupled mode with Z changed. (b) The root locus plot in decoupling mode with Z changed.

three poles in the coupling, one pair of conjugate poles is distributed near the zero axis, and after the decoupling is added, only one pole is distributed on the left side of the 0 axis, and the stability is enhanced.

5. SIMULATION AND EXPERIMENTAL VERIFICATION

5.1. Simulation Analysis

In order to verify the above analysis results, the correctness of the simulation argumentation analysis and the effectiveness of the decoupling method are established in MATLAB/Simulink. The parameters are shown in Table 1.

Figure 15(a) shows the simulation of the grid-connected line resistance $R = 0.3\,\Omega$ when the relative inductance is not negligible. The active power P is set to 5 kW at 0.2 s and set to 0 W at 0.5 s. At this time, a large coupling overshoot occurs in the reactive power, and a steady state error occurs at steady state, in which the control is invalid for the control system at this time. Figure 15(b) shows the

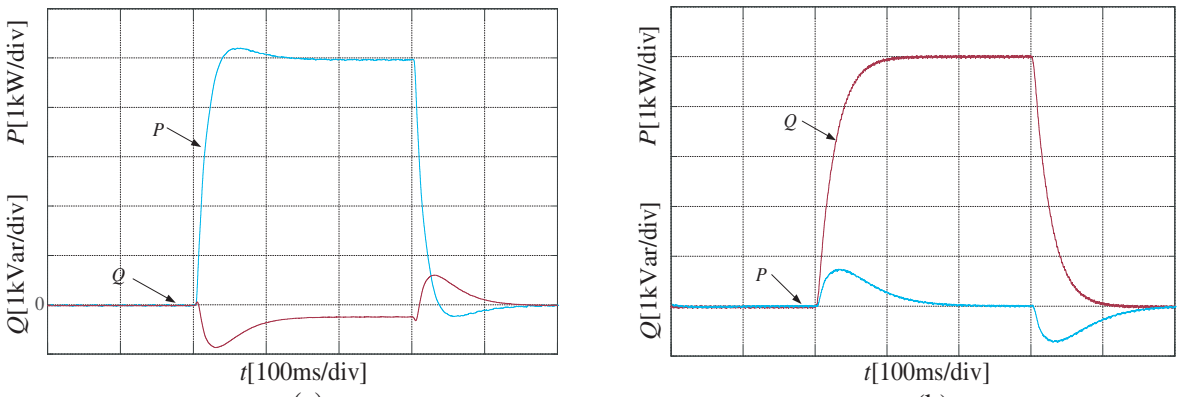

(a) (b)

Figure 15. Power regulation. (a) $R = 0.3\,\Omega$. The active power set to 5 kW then decrease to 0. (b) $R = 0.3\,\Omega$. The reactive power set to 5 kW then decrease to 0.

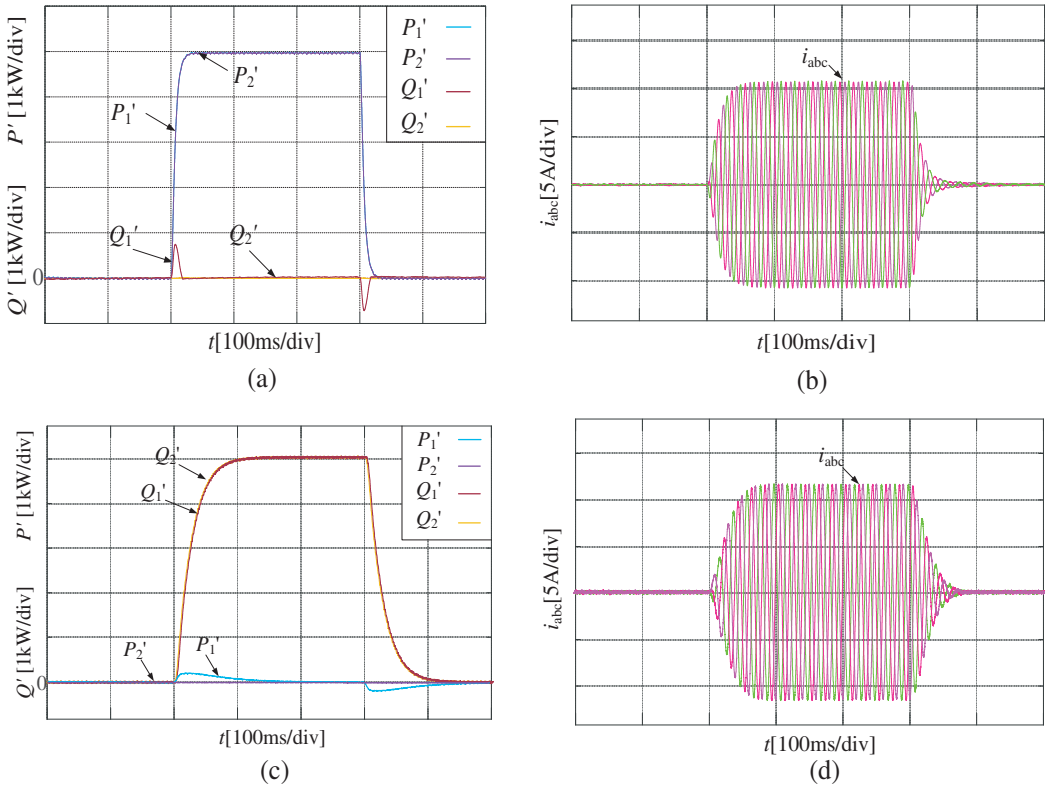

Figure 16. The power regulation when series compensation added and current plot. (a) $R = 0.3\,\Omega$. The compared plot when active power regulation. (b) The current graphic when active power regulation. (c) $R = 0.3\,\Omega$. The compared plot when reactive power regulation. (d) The current graphic when reactive power regulation.

simulation graph when the reactive power is set to 5 kVar at 0.2 s and 0 Var at 0.5 s. It can be seen from the figure that the active power also has a large coupling overshoot during dynamic adjustment.

Figure 16(a) shows the simulation graph when the active power is set to 5 kW at 0.2 s and 0 W at 0.5 s after the coordinate transformation. The active power and reactive power of the feedback control algorithm are both virtual active and reactive. It can be seen from the graph that the virtual reactive power coupling overshoot is effectively suppressed, and the coupling steady-state error during active adjustment can also be eliminated. However, the dynamic coupling at this time is not completely eliminated. Q_2' is a simulation result graph after increasing the series compensation. It can be seen that the coupling overshoot is completely suppressed, which proves the correctness of the dynamic coupling analysis and the effectiveness of the decoupling method, and Figure 16(b) shows the inverter output current graph at power regulation at this time.

Figure 16(c) shows the simulation results when the reactive power is set to 5 kVar at 0.2 s and 0 Var at 0.5 s. P_1' is the simulation graph after increasing the coordinate transformation. It can be seen from the figure that the power is active at this time. The power dynamic coupling overshoot is reduced by nearly 65%, and P_2' is the simulation graph after the series compensation decoupling according to the analysis of Section 3. It can be seen that the dynamic coupling overshoot at this time is also effectively suppressed. Figure 16(d) shows the current graph when the power is adjusted.

5.2. Experimental Analysis

In order to verify the theoretical analysis and simulation results, an experimental platform was built. Figure 17 shows the experimental platform. The main control DSP uses TMS320F2812. The sampling frequency is 20 kHz, and the switching frequency is 20 kHz. Figure 19(a) shows the voltage and current

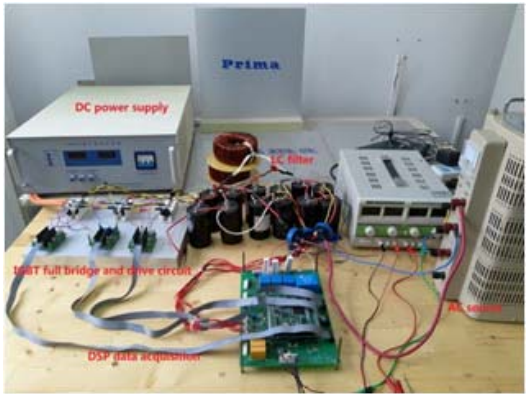

Figure 17. The experiment platform.

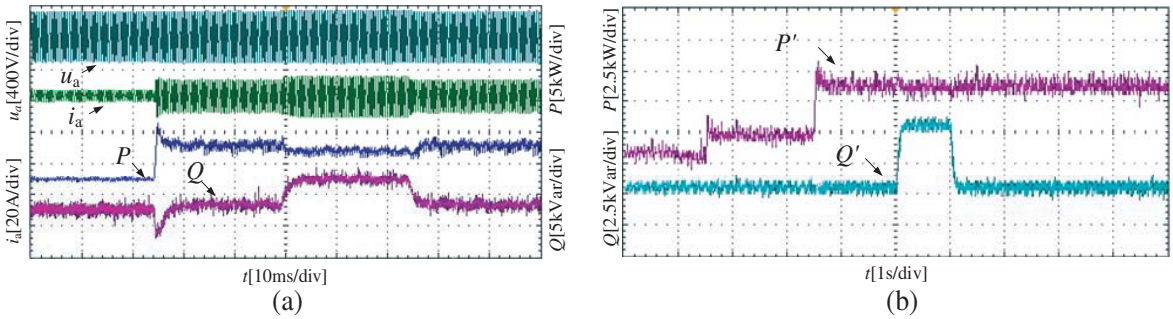

Figure 18. Experimental power regulate graph. (a) The power regulate in undecoupled mode. (b) The power regulate in decoupling mode.

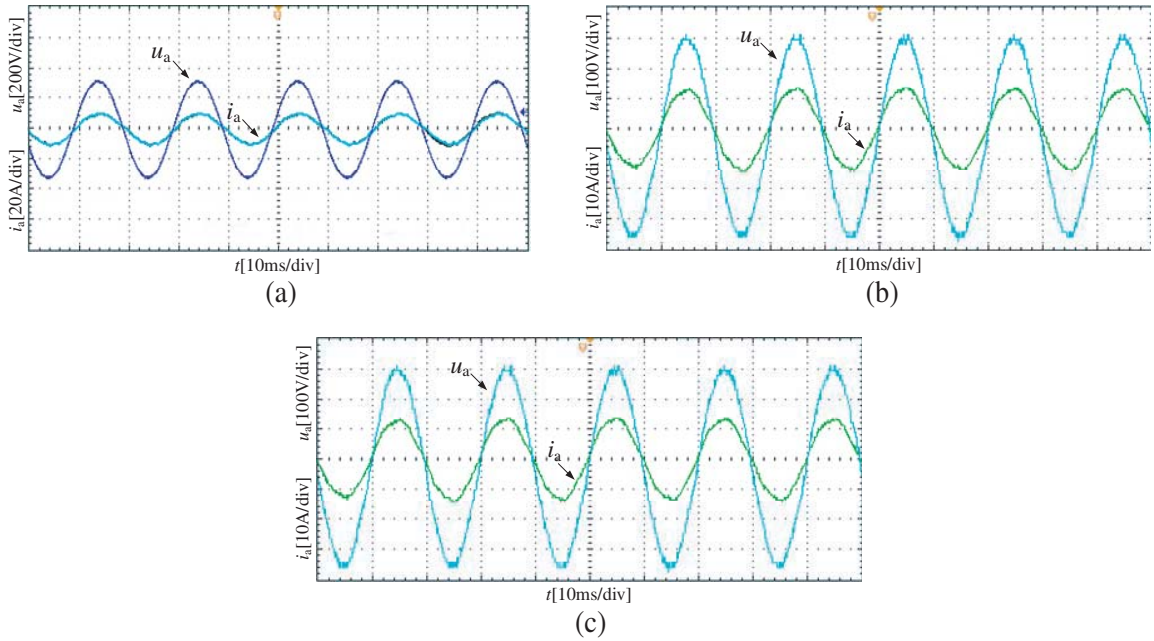

Figure 19. Experimental current graph. (a) The voltage and current plot when synchronize to power grid. (b) The voltage and current plot when only active power export. (c) The voltage and current plot when both active and reactive power export.

waveforms during the grid-connected process.

Figure 18(a) shows the power adjustment pattern and the output voltage and current graph when no decoupling measures are applied. The active power is set to 5 kW at 1 s, and the reactive power is set to 5 kVar at 2 s. It can be seen from the experimental diagram that the coupling overshoot is large during the power adjustment process when no decoupling measures are applied, which seriously affects the dynamic performance. Figure 18(b) shows the power adjustment waveform after adding decoupling measures. The active power is set to 2 kW at 1.5 s, and the reactive power is set to 5 kW at 3.5 s. The reactive power set to 5 kVar at 5 s, and the reactive power set to 0 at 6 s. It can be seen from the experimental graph that the coupling overshoot is effectively suppressed, thus verifying the correctness of the theoretical analysis.

Figure 19(b) shows the current-voltage graph when only active power is output. It can be seen that the phase angle between voltage and current is 0. Figure 19(c) shows the voltage-current graph when only reactive power is output. At this time, there is a phase angle difference between them.

6. CONCLUSION

Distributed energy generation technology is an effective solution to today's energy crisis and environmental problems, but excessive distributed energy grids have a great impact on the structure of the grid. VSG technology is an effective way to solve this problem. However, due to the coupling between powers in the VSG power regulation process, the dynamic performance of the system is affected. This paper analyzes the main factors causing power coupling and adopts decoupling measures. The conclusions are as follows:

(1) When the relative inductance of the grid-connected line is not negligible, the degree of coupling is greatly increased, and the occurrence of steady-state error causes the failure of the control.

(2) The coordinate transformation obtained by grid-connected impedance can suppress the dynamic coupling overshoot to some extent, eliminate the coupling caused by the resistor, eliminate the steady-state error, and improve the power dynamic adjustment performance of the feedback back VSG algorithm.

(3) The small-signal analysis method is used to obtain the coupling relationship between the active loop and reactive loop, so that the entire VSG small-signal model can be obtained. The coupling between the loops can be seen from the entire VSG structure diagram, and decoupling can be achieved by series compensation.

REFERENCES

1. Gao, Y. and Q. Ai, "Hierarchical distributed coordination control of active distribution network with sparse communication in micro-grid networks," *Automation of Electric Power System*, Vol. 4, 019, 2018.
2. Geng, M., Y. Ding, Y. Wang, et al., "Micro-net-"Organic Cells" in the future energy internet system," *Automation of Electric Power Systems*, Vol. 41, No. 19, 1–11, 2017.
3. Han, Z.-X., *Power System Analysis*, 1993.
4. Raj, D. C. and D. N. Gaonkar, "Frequency and voltage droop control of parallel inverters in microgrid," *2016 IEEE 2nd International Conference on Control, Instrumentation, Energy & Communication (CIEC)*, 407–411, 2016.
5. Zhong, Q. C. and G. Weiss, "Synchronverters: Inverters that mimic synchronous generators," *IEEE Transactions on Industrial Electronics*, Vol. 58, No. 4, 1259–1267, 2011.
6. Natarajan, V. and G. Weiss, "Almost global asymptotic stability of a grid-connected synchronous generator," arXiv preprint arXiv:1610.04858, 2016.
7. Natarajan, V. and G. Weiss, "Synchronverters with better stability due to virtual inductors, virtual capacitors and anti-windup," *IEEE Transactions on Industrial Electronics*, Vol. PP, No. 99, 1–1, 2017.

8. Li, D., Q. Zhu, S. Lin, et al., "A self-adaptive inertia and damping combination control of vsg to support frequency stability," *IEEE Transactions on Energy Conversion*, Vol. 32, No. 1, 397–398, 2017.
9. Zhong, Q. C., P. L. Nguyen, Z. Ma, et al., "Self-synchronized synchronverters: Inverters without a dedicated synchronization unit," *IEEE Transactions on Power Electronics*, Vol. 29, No. 2, 617–630, 2014.
10. Wu, H., X. Ruan, D. Yang, et al., "Small-signal modeling and parameters design for virtual synchronous generators," *IEEE Transactions on Industrial Electronics*, Vol. 63, No. 7, 4292–4303, 2016.
11. Dong, S. and Y. C. Chen, "Adjusting synchronverter dynamic response speed via damping correction loop," *IEEE Transactions on Energy Conversion*, Vol. PP, No. 99, 1–1, 2017.
12. Qu, K., W. Li, T. Ye, et al., "Decoupled control strategy of LCL inverter based on state feedback," *Transactions of China Electrotechnical Society*, Vol. 31, No. 20, 130–138, 2016.
13. Peng, Q., H. Pan, Y. Liu, et al., "Design of double closed loop decoupling controller for LCL three phase grid-connected inverter," *Journal of China Electrotechnical Society*, Vol. 29, No. 4, 103–110, 2014.
14. Ye, Z. and X. Yan, "Analysis of power coupling characteristics of microgrid and decoupling control," *Grid Technology*, Vol. 40.3, 812–818, 2016.
15. Li, B., L. Zhou, X. Yu, et al., "New control scheme of power decoupling based on virtual synchronous generator," *IEEE Power and Energy Conference at Illinois*, 1–8, 2016.
16. Li, B., L. Zhou, X. Yu, et al., "Improved power decoupling control strategy based on virtual synchronous generator," *Iet Power Electronics*, Vol. 10, No. 4, 462–470, 2017.
17. Li, W., J. Wang, H. Yang, et al., "Power dynamic coupling mechanism and synchronization frequency resonance suppression strategy of virtual synchronous generator," *Proceeding of the CSEE*, Vol. 37, No. 2, 381–390, 2017.
18. Akagi, H., H. Watanabe, and M. Aredes, *Instantaneous Power Theory and Applications to Power Conditioning*, IEEE Press, New Jersey, 2007.
19. Chen, X., X. Ruan, D. Yang, et al., "Step-by-step controller design of voltage closed-loop control for virtual synchronous generator," *IEEE Energy Conversion Congress and Exposition*, 3760–3765, 2015.
20. Zhang, P., H. Zhao, H. Cai, et al., "Power decoupling strategy based on 'virtual negative resistor' for inverters in low-voltage microgrids," *IET Power Electronics*, Vol. 9, No. 5, 1037–1044, 2016.
21. Wu, T., Z. Liu, J. Liu, et al., "A unified virtual power decoupling method for droop-controlled parallel inverters in microgrids," *IEEE Transactions on Power Electronics*, Vol. 31, No. 8, 5587–5603, 2016.
22. De Brabandere, K., B. Bolsens, D. K. J. Van, et al., "A voltage and frequency droop control method for parallel inverters," *Pesc Record-IEEE Power Electronics Specialists Conference*, 1107–1115, 2004.
23. Erickson, R. W. and D. Maksimovic, *Fundamentals of Power Electronics*, Springer Science & Business Media, 2007.
24. Hu, S., *Principle of Automatic Control*, 2001.
25. Li, Y., X. Ruan, D. Yang, et al., "Modeling, analysis and design for hybrid power systems with dual-input DC/DC converter," *IEEE Energy Conversion Congress and Exposition, 2009. Ecce.*, 3203–3210, 2009.